Hydrogen gas sensing properties of mechanochemically dispersed platinum on α-Fe_2O_3 support

Monika Šoltić[a], Zoltán Klencsár[b], Goran Dražić[c], Marijan Gotić[a], Mile Ivanda[a], Nikola Baran[a,*]

[a]*Laboratory for Molecular Physics and Synthesis of New Materials, Division of Materials Physics, Ruđer Bošković Institute, Bijenička cesta 54, Zagreb, 10 000, Croatia*
[b]*HUN-REN Centre for Energy Research, Konkoly-Thege Miklós út 29-33, Budapest, 1121, Hungary*
[c]*Department of Materials Chemistry, National Institute of Chemistry, Hajdrihova 19, Ljubljana, SI-1001, Slovenia*

Abstract

We investigated the H_2 sensing performance of pure α-Fe_2O_3 and Pt/α-Fe_2O_3 samples, where platinum was mechanochemically dispersed on reducible α-Fe_2O_3 supports by ball miling, at concentrations of 1, 3, 5 and 10 mol%. The hematite nature of the supports was confirmed by Mössbauer spectroscopy. Raman spectroscopy reveals signature lines of hematite as well as "forbidden" longitudinal optical modes indicating stress-induced asymmetry. Scanning and transmission electron micrographs show nanometer-sized Pt dots dispersed on loosely aggregated α-Fe_2O_3 crystallites with a diameter of $\gtrapprox$ 50 nm.

Pt/α-Fe_2O_3 powder was suspended in ethanol and drop-cast onto glass substrates with interdigitated electrodes. The samples were exposed to H_2 concentrations from 0 - 500 ppm at different temperatures from 293 K to 553 K.

The electrical resistance of the samples with Pt decreased with increasing H_2 concentration even at room temperature, indicating sensitivity to H_2. The sensitivity and response time improved significantly at higher temperatures. The response and response time at 100 ppm H_2 ranged from ∼-10% and $\gtrapprox$75 s at 298 K to ∼-50% and ∼5 s at 553 K. No dependence of the sensitivity on the Pt loading was observed, but a Pt loading of at least 1 mol% is essential for the sensors to function. The behavior of the sensors suggests a reversible sensing mechanism based on the Pt-mediated interaction of H_2 with adsorbed oxygen. These results indicate a possible use of Pt/α-Fe_2O_3 as a sensor for H_2 with a linear response at concentrations of 0-100 ppm and encourage further research.

Keywords: sensors, hydrogen, gas sensing, hematite, iron oxide, platinum

1. Introduction

The natural carbon cycle (Berner, 2003; Archer, 2008) is a very complex system that was and still is the key to the existence of life on Earth. Its balance has been disturbed by human activities such as the increase in agriculture and industry, which has led to an increase in CO_2 concentration in the atmosphere (Falkowski et al., 2000), resulting in global warming and ocean acidification (e.g. Guinotte and Fabry (2008); Doney et al. (2009)). The ongoing efforts to counteract these effects are also reflected in scientific research, among others in the field of renewable and sustainable energy. This is evidenced by the growing number of articles[1] on renewable energy over in last three decades; 1990-2000: 159000, 2001-2010: 710000, 2011-2020: 1070000. Fossil fuel technology, while reliable and mature, is not desirable due to its carbon footprint. At the same time, novel solutions for energy generation and storage still need to be drastically improved in order for these technologies to reach a level of usability and reliability comparable to fossil fuel technology.

One of the most important types of energy generation and storage in this context are solar, hydrogen and fuel cell technology (Ogden, 2002; Aroutiounian, 2007), the development of which has been ongoing for almost 50 years (Aroutiounian, 2007). The safe storage and transfer of hydrogen is one of the most important issues, which is particularly problematic due to the physical and chemical properties of hydrogen. Under standard conditions, hydrogen is a colorless and odorless gas that cannot be perceived visually or olfactorily. At time same time, in concentrations between 4% and

*Corresponding author
Email address: nikola.baran@irb.hr (Nikola Baran)
[1]as indexed by Google Scholar at the time of writing

74% in the air, it can ignite with an energy threshold of only 0.02 mJ (Lewis and von Elbe, 1987), which makes it extremely unsafe. To avoid incidents, close tolerances and high-quality materials must be used in the manufacture of hydrogen system components. They must also be equipped with redundant, fail-safe subsystems that can reliably detect hydrogen leaks long before the hydrogen concentration reaches unsafe limits.

The detection of hydrogen gas leaks in a growing number of applications requires affordable, reliable and safe hydrogen sensor arrays. Hydrogen sensors have been extensively investigated and can be classified into different categories depending on the detection principle. In a review by Li et al. (2018), they are divided into three main categories: electrochemical (Korotcenkov et al., 2009), optical (see Pathak et al. (2023) for review) and chemiresistor (Koo et al., 2020; Majhi et al., 2021), while Hübert et al. (2011) list eight categories: catalytic, thermal conductive, electrochemical, resistance-based, work function based, mechanical, optical and acoustic. Chemiresistor types, as described by Li et al. (2018), are currently the most interesting due to their long-term stability. They typically consist of a platinum, palladium or Pt/Pd alloy material, which serves as the transducer platform, and the acceptor (support) material, usually in the form of a metal oxide semiconductor (MOS) (Aroutiounian, 2007; Gu et al., 2012; Li et al., 2018). Various MOSs are being researched for this purpose, including SnO_2 (Maksimova et al., 2021; Duoc et al., 2024) and WO_3 (Shrisha et al., 2023; T et al., 2024).

More complex MOS-based nanocomposites are also under development, not only for the detection of hydrogen (Wang et al., 2023), but also for other analytes such as organic vapors. For example, Zhang et al. (2023) report on the performance of room temperature ethanol sensors made of In_2O_3/ZnO/$Ti_3C_2T_X$ MXene derived from metal-organic frameworks. Sun et al. (2024) produced zinc metasannate ($ZnSnO_3$) - zinc oxide nanofibers and coupled them with $Ti_3C_2T_X$ MXene sheets to improve acetone sensing performance. Similarly, Xie et al. (2024) use the same MXene to prepare In_2O_3 nanofibers for the detection of trimethylamine at low temperatures (~400 K).

Pt and Pd have also been investigated in the context of gas sensors with carbon support material in different morphologies; e.g., nanotubes (Penza et al., 2008), graphene (Wu et al., 2023), and fullerene (Xu et al., 2021). Currently, the commercial market for hydrogen sensors is dominated by ZnO-based MOS with response times between 4 to 20 s (Hübert et al., 2011). However, there is still a great need for more affordable sensors with shorter response times and lower power consumption.

Hematite or α-Fe_2O_3 has attracted much attention due to its affordability and ease of synthesis and has become a basic material for various technological applications due to its low toxicity and exceptional chemical stability. It offers advantages such as cost efficiency and environmental compatibility. Moreover, Fe_2O_3 exists in two interchangeable crystalline forms, α-Fe_2O_3 and $\gamma-Fe_2O_3$, with the former being the most stable under atmospheric conditions (Pourmadadi et al., 2022). α-Fe_2O_3 is promising for photoelectrochemical (PEC) water splitting due to its stability in water, its non-toxic properties and its suitable band gap (Kraushofer et al., 2018). In addition, it has been intensively explored as a potential anode material for Li-ion batteries (Sun et al., 2010), offering advantages such as high theoretical capacity and corrosion resistance (Reddy et al., 2007; Li et al., 2023). Its wide exploration extends to areas such as magnetic devices, photocatalysis, gas sensing and energy storage applications (Ghule et al., 2022).

A number of advantages make α-Fe_2O_3 interesting MOS material for sensor technology. It is inexpensive, can be synthesized in different morphologies and can be reduced. The reducible support material interacts with the dispersed platinum and influences its oxidation states, which should improve the determination of the catalytic activity and stability of Pt/α-Fe_2O_3 catalysts (An et al., 2011). An et al. (2011) estimated the interaction energy of Pt-Fe_2O_3 to be ~72 eV based on XPS data. Wang et al. (2014) investigated the metal-oxide interface effects between nanometer-sized Pt particles on mesoporous SiO_2, Co_3O_4, MnO_2, NiO_2, CeO_2, and Fe_2O_3. They conclude that the reaction rates in the gas phase are drastically influenced by the interactions between the Pt nanoparticles (PtNPs) and reducible metal oxide supports. The interaction energy of other types, e.g. carbon supports with Pt, is less pronounced. For example, Ma et al. (2015) reported a binding energy between Pt and graphene (G;-1.15 eV), low (LOG;-2.67 eV to -7.85 eV) and highly oxidized graphene (HOG;-1.89 eV to -2.01 eV) calculated using density functional theory. To improve the interaction energy, the carbon supports can be doped with nitrogen (N), resulting in -2.74 eV for G-1N, -2.43 eV for G-3N, -2.8 eV for LOG-N and -2.16 eV for HOG-N.

Gas sensors based on α-Fe_2O_3 have been studied for at least three decades (e.g., Nakatani and Matsuoka (1982)). Earlier work focused mainly on sensors based on doped α-Fe_2O_3 (e.g, Saritas et al. (2018)). For example, Picasso et al. (2014) investigated Pd-doped α-Fe_2O_3 sensors for petroleum gas, while Wang et al. (2007) and Guo et al. (2018) investigated the H_2S sens-

ing properties of Pt-doped α-Fe_2O_3.

To improve the gas sensing performance, numerous studies have focused on the development of hematite with different morphologies, sizes and shapes (Muhajir et al., 2019). In particular, nanoscale structures of α-Fe_2O_3 show better performance due to their large surface-to-volume ratio and increased surface reactivity. Various synthesis techniques have been applied to prepare α-Fe_2O_3 with different structures, including nanorods, nanowires, nanosheets and more, to optimize its performance for different applications.

Lei et al. (2023) synthesized Pt-doped mesoporous α-Fe_2O_3 microspheres using a solvothermal method for the detection of acetone and characterized them using various techniques. By controlling the amount of Pt, they found that the α-Fe_2O_3 doped with 2 at% Pt exhibits superior sensing performance, with a response of 105 to 100 ppm acetone at 175°C, a 2.5-fold improvement over pure α-Fe_2O_3, and can even detect 20 ppb acetone with a response of 1.24 at the same temperature while maintaining performance at high humidity, highlighting its potential for acetone detection in human breath.

Umar et al. (2021) synthesized cubic-shaped α-Fe_2O_3 microstructures by hydrothermal technique from hydrated ferric nitrate, hexamethylenediamine and sodium hydroxide and investigated their electrocatalytic effect on ethanol gas, H_2 and CO. The morphology, composition and structure of the synthesized microstructure were confirmed by field emission scanning electron microscopy, X-ray diffraction, energy dispersive spectroscopy and Fourier-transform infrared spectroscopy. The α-Fe_2O_3 powder was dispersed in deionized water and deposited on the surface of an alumina substrate with interdigitated Au electrodes. The sensors showed a gas response to ethanol of 13.1 and a response to 100 ppm H_2 of ~1.71 at 400°C.

Ma et al. (2020) synthesized Pt/FeO_x heterostructures, including Pt/Fe_2O_3 and Pt/Fe_3O_4 nanospheres, by hydrothermal methods and subsequent in situ reduction in ethylene glycol solutions and showed different catalytic activities for CO oxidation. The Pt/Fe_3O_4 nanospheres showed superior catalytic performance due to strong interactions between electronics and metal support, which facilitate oxygen activation and chemisorption at the surface. The characterization techniques revealed a uniform distribution of PtNPs on FeO_x supports, with Pt/Fe_3O_4 exhibiting enhanced oxygen activation, which is crucial for CO oxidation, highlighting the importance of interactions between platinum and reducible supports in catalytic processes.

α-Fe_2O_3-based H_2 sensors are also the subject of studies. Hara and Nishida (1994) prepared α-Fe_2O_3 thin films by high-frequency (RF) sputtering and doped them with TiO_2 and MgO to produce H_2 gas sensors with a sensitivity of ~60% at 3000 ppm and 420°C. Similarly, Lim et al. (2001) prepared Pt-doped γ−Fe_2O_3 H_2 sensors by plasma-enhanced chemical vapor deposition (PECVD) and reported sensitivities of ~90% at 500 ppm for pure γ−Fe_2O_3 and ~80% for Pt-doped γ−Fe_2O_3, while at 3000 ppm the reported sensitivities were 96% (γ−Fe_2O_3) and 88% (Pt-γ−Fe_2O_3). The experiments were conducted at slightly lower temperatures of 300°C, and no improvement in H_2 sensitivity was observed with Pt doping. Furthermore, their work clearly illustrates the above-mentioned interaction between Pt and the reducible Fe_2O_3 support. The support reduces to Fe_3O_4, which in turn can oxidize to γ−Fe_2O_3.

We find that Pt solid-state dispersions on α-Fe_2O_3 are not sufficiently addressed in the literature, especially in the field of sensors, where the favorable Pt-α-Fe_2O_3 interaction could play a role in sensor performance. This is even more true for systematic research to investigate the effect of Pt loading on sensor properties. Another question that comes to mind when reading the above papers in this field is the reliability and repeatability of the results. On the one hand, Hara and Nishida (1994) report on the influence of doping on sensor sensitivity, but no error bars are given. On the other hand, Lim et al. (2001) clearly show the error bars, but do not specify how they were determined and how the degree of Pt doping is determined. Umar et al. (2021) clearly present their results, but it also remains unclear how stable the sensors are with repeated measurements.

In this paper, we present a study on the H_2 sensing properties of Pt/α-Fe_2O_3 samples, where Pt was mechanochemically dispersed on the α-Fe_2O_3 support in a ball mill, resulting in a solid state-dispersion. We also use synthesis methods that do not require expensive and complex equipment, such as the aforementioned RF sputtering and PECVD. The dependence of the response time and sensitivity on sensor temperature and Pt concentration are systematically analyzed and clearly presented, as well as the stability of the results with repeated measurements. We believe that this adds considerable scientific value to this work.

2. Materials and methods

2.1. Chemicals

Iron(II)acetate, platinum(II)acetylacetonate, ethanol, and anhydrous toluene, manufactured by Sigma Aldrich were used as received.

2.2. Synthesis of the samples

The α-Fe_2O_3 supports and Pt/α-Fe_2O_3 samples were synthesized according to the procedure described in Marić et al. (2023). Briefly, Fe(II)acetate was ground in a *Fritsch Pulverisette 7 premium line* planetary mill with 40 hardened stainless steel balls at 400 rpm for two hours. After grinding, the resulting orange-red powder was heated in an argon stream at 473 K for 30 minutes, in an argon stream at 673 K for 30 minutes, in an argon stream at 873 K for 1 hour, and in an oxygen stream at 873 K for 2 hours in a tube furnace; a dark red powder (α-Fe_2O_3 support) was obtained.

The platinum was dispersed by mixing the α-Fe_2O_3 support with 1, 3, 5, and 10 mol% $Pt(acac)_2$ powder precursors previously dissolved in a certain volume of toluene. The paste obtained was homogenized in a planetary ball mill with stainless steel balls at a speed of 400 rpm for two hours and annealed in an argon stream for one hour and in an oxygen stream at 673 K for two hours. The samples are labeled as follows FP-1, FP-3, FP-5 and FP-10, where F represents the α-Fe_2O_3 support, P represents platinum and the numbers 1, 3, 5, and 10 mol% represent the mechanochemically dispersed Pt on the α-Fe_2O_3 support.

2.3. Instrumental analysis

The atomic resolution scanning transmission electron microscope (AR STEM), model Jeol ARM 200 CF, with an emission voltage of 200 kV, coupled with the Gatan Quantum ER system and with electron energy loss spectroscopy and energy dispersive X-ray spectrometry (Jeol Centurio 100), Tokyo, Japan, was used to determine the morphology of the samples, as well as the thermal field emission scanning electron microscope (FE-SEM), model JSM-7000F, manufactured by JEOL Ltd. connected to the EDS/INCA 350 (energy dispersive X-ray analyzer) from Oxford Instruments.

Mössbauer spectra were collected in transmission geometry using a standard instrumental configuration by *WissEl GmbH* (Starnberg, Germany). ^{57}Co in rhodium matrix was used as a source of radiation. The spectrometer was calibrated using a standard spectrum of α-Fe foil at room temperature.

A Renishaw inVia Raman spectrometer with Renishaw Centrus detector was used to record the Raman spectra of the samples. The samples were irradiated with a power of 0.645 mW from a 785 nm laser for 32 accumulations of 1 s duration. The samples were placed in a Linkam THMS 600 cell with temperature control Linkam Scientific Instruments Ltd TMS 94 connected to a Gometrics Industrial Gas Mixer. The gas mixer delivered 1000 SCCM streams of synthetic air (S.A.) and H_2 mixtures. The spectra were recorded in S.A. with and without 250 ppm H_2 at 298 K and 553 K. The microscope connected to this Raman spectrometer was used to generate the optical microscope image in Fig. 1 on the left.

2.4. Drop-casting

In order to measure the electrical response of the prepared α-Fe_2O_3 and Pt/α-Fe_2O_3 samples, they must be connected to an electrical circuit. For that purpose, we obtained interdigitated gold electrodes (IDE) from *Micrux Technologies* (model *ED-IDE2-Au* with 10/5 µm, electrode/gap). Once the powdered α-Fe_2O_3 and Pt/α-Fe_2O_3 samples were suspended in ethanol (0.01 g in 40 μL), they were drop cast onto IDE substrates. The volume of the suspension was carefully chosen to avoid underfilling or overfilling the circular area with the IDE background (see Fig. 1, right).

In order to minimize the possible influence of the sample structure on the sensing performance of the samples, a precision drop casting system was built in-house. It consists of a heated IDE substrate holder with 4 axes (2 translation + 2 tilt angles), a pipette attached to a stepper motor driven vertical axis and a loupe with adjustable zoom and illumination. This enables precise control of the drop casting process, prevents sample leakage and ensures uniform layers.

The IDE substrate was positioned on the holder heated to 328 K, with the circular area with IDE coating (see Fig. 1, left side) coaxial to the pipette. The optimum temperature to which the substrate was heated was determined empirically. It allows the ethanol to evaporate just enough for the suspension to reach the edge of the circular area with IDE coating without creating inhomogeneities. Thus, the produced coatings fall into Zone II (uniform deposition) as described by Kaliyaraj Selva Kumar et al. (2020) in Fig. 9e and Ta et al. (2016) in Fig. 6b, although they used laser-induced evaporation. At substrate temperatures below 328 K, the sample leaked outside the circular region, while at higher temperatures the ethanol evaporated too quickly and formed a spot smaller than the circular region, leaving much of the IDEs uncovered. To prevent the sample from leaking, the substrate was also carefully lifted in both axes. The suspensions of α-Fe_2O_3 and Pt/α-Fe_2O_3 were then sonicated for 2 - 3 minutes to ensure their homogeneity before being placed in a pippette and dropped onto the substrate from a fixed height of 5 mm. This distance was chosen after extensive testing and proved to be the minimum distance required to reliably release the drop

from the pipette without causing splashing. As an additional measure to ensure homogeneity and to avoid sedimentation, the suspension was not allowed to remain in the pipette for more than a total of 5 seconds. After the sample was dropped onto the substrate, it was left on the heated holder to dry, which took ~10 s. This method was used to produce samples suitable for gas sensing tests, as shown in the center panel of Fig. 2.

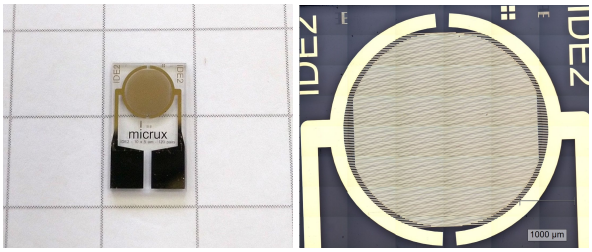

Figure 1: *Left*: Interdigitated electrode (IDE) substrate used in the drop-casting of the α-Fe_2O_3 and Pt/α-Fe_2O_3 samples. *Right*: IDE-backed area of the substrate under the light microscope.

Figure 2: *Left*: Underfilled sample cast at a too high temperature. *Center*: Substrate homogeneously filled with Pt/α-Fe_2O_3 sample. *Right*: Overfilled sample that spilled cast at a too low temperature.

We would like to emphasize at this point that the step of depositing the α-Fe_2O_3 and Pt/α-Fe_2O_3 samples onto the IDE substrates has proven to be very sensitive and difficult process in the context of gas sensor production. Any slight undercoating, overcoating or inhomogeneity (as in coffe rings Kaliyaraj Selva Kumar et al. (2020)) of the sample covering the circular area with IDE coating resulted in gas sensor measurements that were not comparable to other samples or samples that did not respond at all. Therefore, the circular area with IDE background had to be homogeneously covered with sample suspension up to the edge. Despite extensive efforts to improve the repeatability of the drop-casting procedure, not all samples met the above criteria. These samples were completely discarded together with the corresponding substrates. Examples are shown in Fig. 2 (left and right panels). For clarification, only the substrates that were homogeneously filled with α-Fe_2O_3 or Pt/α-Fe_2O_3 samples up to the edge of the circular area coated with IDE were further analyzed as gas sensors (shown in the center panel of Fig. 2).

2.5. Gas sensing measurements

To measure the response of the samples to the presence of hydrogen gas, we used a home-built chamber as in our previous work (Baran et al., 2022), upgraded with a heated sample stage. It is designed to isolate the analyzed sample from the outside atmosphere, vibrations and electromagnetic disturbances. The sample stage is equipped with a heater, a thermistor and two gold-plated probes. The temperature was controlled and monitored from a PC via a special electronic circuit board and stabilized to ± ~1 K. The probes were connected to a *Keithley Sourcemeter 2450* via shielded cables. The *SourceMeter* was programmed to measure resistance while delivering a constant current.

After the IDE substrate with the sample was positioned on the heating stage, the gold-plated probes were placed on the corresponding contacts of the substrate. After closing the chamber and setting the temperature, the sample was stabilized for ~5 minutes and its resistance was recorded. Then, specific amounts of H_2 gas were injected into the chamber using a calibrated *Hamilton* gas syringe. After each injection, the sample was again left to stabilize. The resistance at each step was recorded and then used to estimate the sensor response.

Gas was added until the sample began to saturate, i.e. the change in resistance did not follow the increasing H_2 concentration. In the samples tested in this work, saturation became evident at ~400 ppm. After reaching saturation, the chamber was ventilated and the measurement procedure was restarted, repeating the measurements for each sample. All measurements were performed in ambient air at 50% relative humidity (RH).

3. Results

3.1. Morphology

Scanning electron micrographs and transmission electron micrographs are shown in Fig. 3 and Fig. 4 to illustrate the morphology of the sample at different scales. The images were obtained using secondary electron microscopy (SEI) at an accelerating voltage of 10 kV and a magnification of 55,000x (FP-1) or 50,000x (all others). The images show that the investigated material consists of α-Fe_2O_3 crystallites with a size of $\gtrapprox$ 50 nm, which tend to form loose aggregates. The α-Fe_2O_3 crystallites did not change in shape and size with Pt loading. However, the SEM was not able to resolve the Pt-loading confirmed by XRD (Marić et al., 2023). For this reason, we used the scanning transmission electron microscope (STEM) with an attached EDS module.

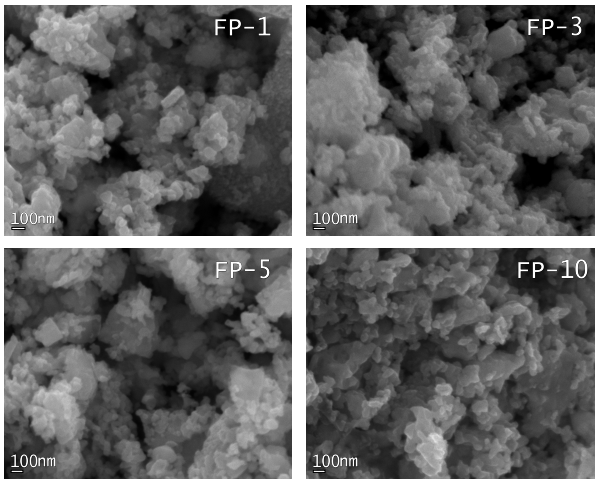

Figure 3: Scanning electron micrographs of FP-1 (*top left*), FP-3 (top right), FP-5 (bottom left), and FP-10 (*bottom right*), taken with secondary electron imaging at an accelerating voltage of 10 kV and a magnification of 55,000x (FP-1) and 50,000x (all others). α-Fe_2O_3 crystallites with a size of $\gtrapprox$ 50 nm are visible in all images. See Sec. 3.1 for more details.

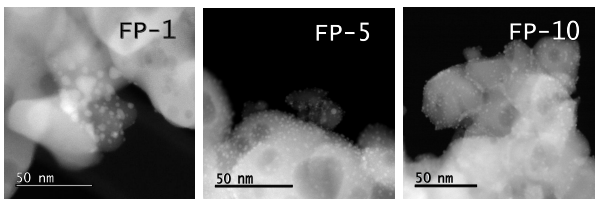

Figure 4: Dark-field scanning transmission electron micrographs of FP-1 (*left*), FP-5 (center), and FP-10 (*right*) showing nanometer-sized crystalline Pt dots (bright dots) on α-Fe_2O_3 crystallites. See Sec. 3.1 for more details.

From the scanning transmission electron microscopy (STEM-DF) dark-field images shown in Fig. 4, it is evident that the crystalline Pt is dispersed in nanometer-sized dots on α-Fe_2O_3, which are visible as bright dots. The α-Fe_2O_3 supporting the Pt dots forms solid, coherent structures with a characteristic cluster diameter of ~50 nm, which are also resolved in SEM images shown in Fig. 3. No significant differences in the dimensions of the Pt dots or α-Fe_2O_3 clusters were observed between the different sample series.

In a previous work (Marić et al. (2023), sec. 3.1), a detailed XRD analysis, including Rietveld refinements, was performed on Pt/α-Fe_2O_3 samples. The analysis showed that even at high platinum loadings of 10 mol%, no platinum maxima could be detected in the XRD patterns. The parameters of the unit cell and the volume-averaged domain sizes of the hematite phase were determined. It is noteworthy that there was no substitution of Fe^{3+} by Pt^{4+} in the hematite. The size of the hematite domains ranged from 60 to 90 nm and remained constant at different Pt loadings. Importantly, the PtNPs were not doped but decorated on the surface of α-Fe_2O_3 by solid-state impregnation, resulting in very small and uniformly dispersed PtNPs that were not visible in the XRD pattern. In addition to the XRD results, Marić et al. (2023) also include the BET nitrogen adsorption–desorption isotherm, the temperature-programmed reduction in hydrogen and XPS spectra of these samples in their study.

3.2. Mössbauer spectroscopy

The ^{57}Fe Mössbauer spectra were fitted using version 4.0i of the MossWinn program Klencsár et al. (1996). The ^{57}Fe isomeric shifts are given with respect to those of α-Fe at room temperature.

Consistently with the results of powder X-ray diffraction of the same samples (Marić et al., 2023), the main component (component A, see Tab. 1) of the ^{57}Fe Mössbauer-spectra is a sextet related to hematite, with Mössbauer parameters corresponding to those of stoichiometric hematite at room temperature (^{57}Fe isomer shift: δ ≃0.37 mm s^{-1}, twice of the first order quadrupole shift: 2ϵ ≃-0.21 mm s^{-1}, hyperfine magnetic field: B_{hf} ≃51.8 T (Ozdemir et al., 2008)). At the same time, the outer (1-6) peaks of the sextet component in question clearly show inwardly directed shoulders, indicating the presence of additional components besides the stoichiometric hematite. The apparently broader peaks responsible for these shoulders are due to another sextet component (component B, see Tab. 1) which shows the effects of the hyperfine parameter distribution caused by the presence of a variety of slightly

different iron microenvironments.We modeled this component by assuming a Gaussian probability distribution in the values of the ^{57}Fe hyperfine magnetic field (B_{hf}) and resorted to the corresponding version of the Voigt-based fit (Rancourt and Ping, 1991) implemented in the MossWinn program. The parameters δ, 2ϵ and mean B_{hf} (see Tab. 1) of component B were assumed to be the same in the different samples, and the spectra were all fitted simultaneously with the corresponding constraint.

In the sample with 1 mol% Pt added, a small singlet component appears in the spectrum, which is similar to that of stainless steel and was modeled with a pseudo-Voigt peak profile (see Fig. 5 and Tab. 1). This component is assumed to originate from the stainless steel balls of the planetary mill used to grind the sample. Compared to stoichiometric hematite, component B exhibits a lower mean hyperfine magnetic field of ~49 T, a lower quadrupole shift of $\epsilon \simeq 0$ mms^{-1}, and a lower isomer shift of ~0.28 mm s^{-1}. The latter values indicate that, with respect to the octahedral oxygen coordination of iron in stoichiometric hematite, the corresponding iron atoms are located as Fe^{3+} in an altered oxygen ligand environment, possibly with tetrahedral oxygen coordination.

Parameters	**FP-0**	**FP-1**	**FP-3**	**FP-5**	**FP-10**
Nominal Pt mol%	0	1	3	5	10
α-Fe_2O_3 (component A, sextet, regular iron microenvironment)					
Relative area, %	86.2(4)	68.9(7)	71.6(9)	78.8(1.4)	88.3(6)
δ, mm s^{-1}	0.3694(4)	0.371(1)	0.372(1)	0.373(2)	0.369(1)
B_{hf}, T	51.233(3)	51.11(1)	51.17(1)	51.12(1)	51.40(1)
2ϵ, mm s^{-1}	-0.211(1)	-0.215(2)	-0.215(3)	-0.213(4)	-0.194(1)
Γ_L, mm s^{-1}	0.308(1)	0.309(3)	0.330(4)	0.343(6)	0.307(2)
α-Fe_2O_3 (component B, VBF sextet with Gaussian distribution in B_{hf}, distorted iron microenvironment)					
Relative area, %	13.8(4)	29.6(7)	28.4(9)	21.2(1.4)	11.7(6)
δ, mm s^{-1}	0.283(2)				
$<B_{hf}>$, T	48.89(3)				
2ϵ, mm s^{-1}	0.008(4)				
$\sigma(B_{hf})$, T	1.01(6)	1.16(5)	1.26(8)	1.2(2)	0.94(11)
Γ_L, mm s^{-1}	0.308(1)	0.309(3)	0.330(4)	0.343(6)	0.307(2)
Stainless steel (singlet, Voigt peak profile)					
Relative area, %		1.4(1)			
δ, mm s^{-1}		-0.09(F)			
Γ_G, mm s^{-1}		0.3(F)			
Γ_L, mm s^{-1}		0.309(3)			

Table 1: α-Fe_2O_3 Mössbauer parameters obtained by simultaneous fit of the spectra shown in Fig. 5. The numbers in parentheses indicate the standard fit error in the last digit(s). The parameter values marked with (F) were fixed during the fit. Values in rows extending over multiple columns were assumed to be identical in the different spectra. δ denotes the ^{57}Fe isomer shift wrt. α-Fe at room temperature, B_{hf} is the hyperfine magnetic field, $<B_{hf}>$ denotes the mean and $\sigma(B_{hf})$ is the standard deviation of the Gaussian probability distribution in B_{hf}, ϵ is the first-order quadrupole shift, Γ_L is the Lorentzian width (FWHM), and Γ_G is the Gaussian width (FWHM) associated with Voigt line profiles. VBF stands for "Voigt Based Fitting" (Rancourt and Ping, 1991). See also Fig. 5 and Fig.6.

The presence of such iron microenvironments may indicate the formation of spinel structures, such as maghemite (Sánchez et al., 2007). However, the relatively large fraction of iron atoms contributing to component B (see Figs. 5,6, as well as Tab. 1), and the simultaneous absence of spinel-associated reflections in the corresponding X-ray diffractograms of Marić et al. (2023) suggest that the microenvironments in question may also form within the hematite structure, presumably due to defects caused by the grinding process.

It is interesting to observe (Fig. 6), that in the Pt-containing samples, the concentration of iron in the microenvironments associated with component B decreases with the increase in Pt concentration. Consequently, the presence of Pt above a concentration of 1 mol% seems to hinder the formation of these altered oxygen-ligand environments of iron.

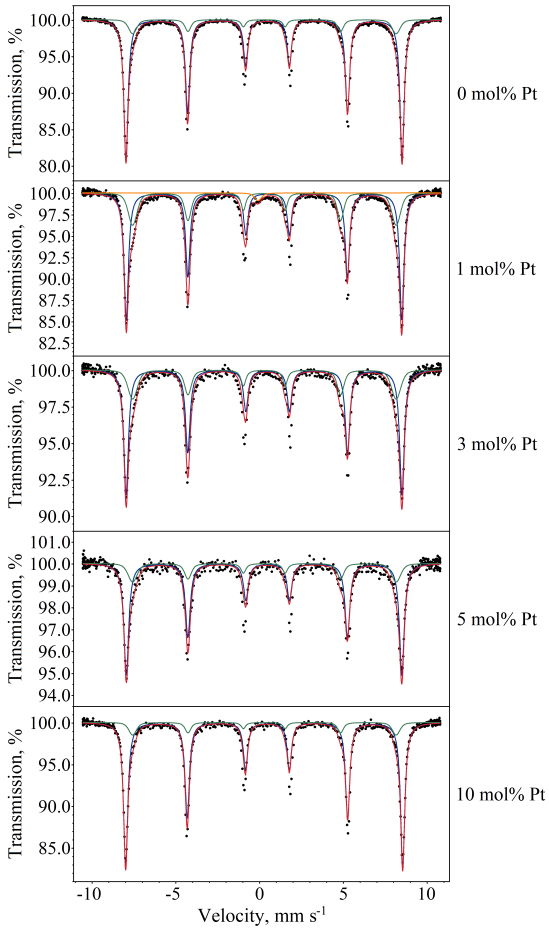

Figure 5: Room temperature ^{57}Fe Mössbauer spectra (circles) of the analyzed samples together with their decomposition into subcomponents (solid line). Next to the spectra, the nominal molar Pt concentrations, used in the preparation of the samples are indicated.

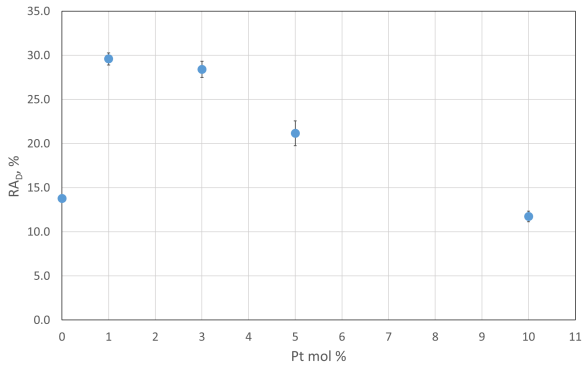

Figure 6: Relative area fraction of the Mössbauer spectral component B (see Tab. 1 and Fig. 5) associated with distorted iron microenvironments in hematite (RA_D) as a function of the nominal Pt content (Pt mol%).

3.3. Raman spectroscopy

Average Raman spectra in streams of S.A. at 298 K and 553 K, and S.A. with 250 ppm of H_2 at 553 K are shown in Fig. 7. The temperatures were chosen to reflect the room temperature and the temperature at which our sensors were most sensitive. The analysis and fitting of Raman spectra was performed using the Renishaw Wire 5.5 software package. By fitting curves of mixed type to the spectra, we found a total of 10 peaks. Their positions are listed in Tab. 2, together with the assignments given in Chamritski and Burns (2005); Jubb and Allen (2010).

Prominent α-Fe_2O_3 signature peaks were found as A_{1g} at 222 cm^{-1} and 491 cm^{-1}, 5 E_g at 240, 288, 295, 402 and 603 cm^{-1}. In addition, the spectra show a "forbidden" Raman peak at 656 cm^{-1} and its overtone at 1299 cm^{-1}. These can be assigned as longitudinal optical (LO) E_u modes (Bersani et al., 1999; Marshall et al., 2020). The presence of the "forbidden" LO E_u mode indicates an asymmetry in the structure of hematite possibly caused by impurities and/or mechanical stress from the ball milling process.

Another broad peak at ~1199 cm^{-1} is visible as a red tail of the 2LO E_u mode at 1294 cm^{-1}, which cannot be reliably assigned and possibly comes from the interaction with PtNPs or impurities. Similar interference peaks were also reported by Bersani et al. (1999) for some naturally occurring hematite crystals and are also visible in the spectra of Marshall et al. (2020). This peak has been denoted with a question mark in the Tab. 2.

Recorded Raman spectra are on average red-shifted by ~8 cm^{-1} compared to the spectra reported in the literature for hematite in the bulk. This is consistent with the results of Luna et al. (2016) for α-Fe_2O_3 nanocrystals and is expected due to phonon confinement in our nanoscale hematite (Radin et al., 2021).

In addition, the spectra recorded at 553 K are on average red-shifted by ~5 cm^{-1} compared to the spectra recorded at 298 K. This is consistent with the results obtained by de Faria et al. (1997); Chamritski and Burns (2005) and is expected due to the thermal expansion and relaxation of the bonds within the lattice. This in turn leads to a shift in vibrational energy levels (Xie et al., 2001).

Assignment	Lit/cm^{-1}	S.A. 298 K	S.A. 553 K	S.A. 553 K + 250 ppm H_2
A_{1g}	225	221.96	220,28	220,28
E_g	247	240.33	236,00	236,00
E_g	293	287.76	283,81	283,76
E_g	299	294.80	290,00	291,68
E_g	412	402.35	398,06	398,09
A_{1g}	498	490.60	486,28	487,29
E_g	613	603.46	598,84	599,03
1LO E_u	660	655.62	646,87	649,81
?	-	1198.52	1132,62	1151,01
2LO E_u	1322	1299.25	1293,54	1294,03

Table 2: Table with the Raman peaks observed in the FP-5 samples at 553 K. The first two columns show the assignments and peak positions listed in the literature, the third column shows the matched peak positions in S.A. at room temperature, the fourth and fifth columns show the matched peak positions at 553 K in S.A. and S.A. with 250 ppm of H_2, respectively. The question mark in the penultimate line indicates a (complex) peak that cannot be reliably assigned. See Sec. 3.3 for details.

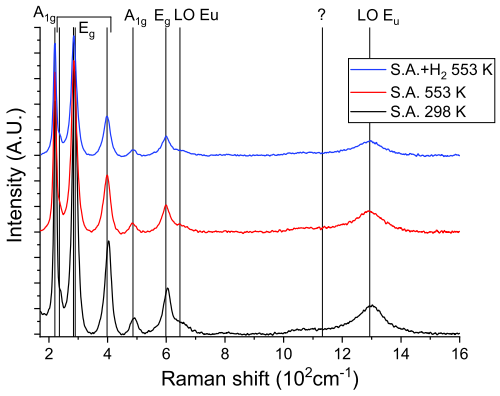

Figure 7: Raman spectra of FP-5 at 298 K in a stream of S.A. and at 553 K in streams of S.A. (red) and S.A. with 250 ppm H_2 (blue).

3.4. Gas sensing properties of Pt/α-Fe_2O_3

As mentioned in Sec. 2.5, we measured the electrical resistance of the samples at sequentially increasing

H_2 gas concentrations and different temperatures. The result is illustrated in Fig.8. We define the response of the sensors as the relative change in their electrical resistance $\Delta R/R_0 = (R - R_0)/R_0$, where R_0 is the initial resistance at the given temperature in air, while R is the resistance measured after exposure to H_2. In this sense, the response curve can be determined by plotting $\Delta R/R_0$ against the H_2 concentration.

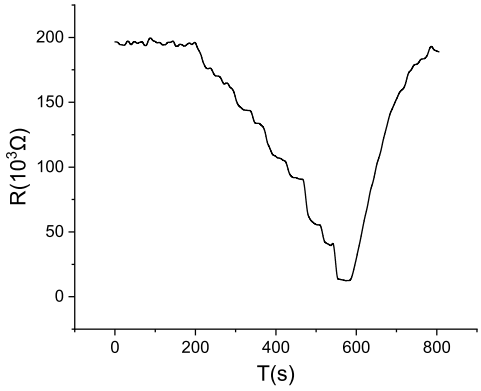

Figure 8: Example of the raw measurement. The sample response to successive increase in the H_2 concentration in the form of step-like decreases in resistance is visible, as is the recovery. See Sec. 3.4 for more details.

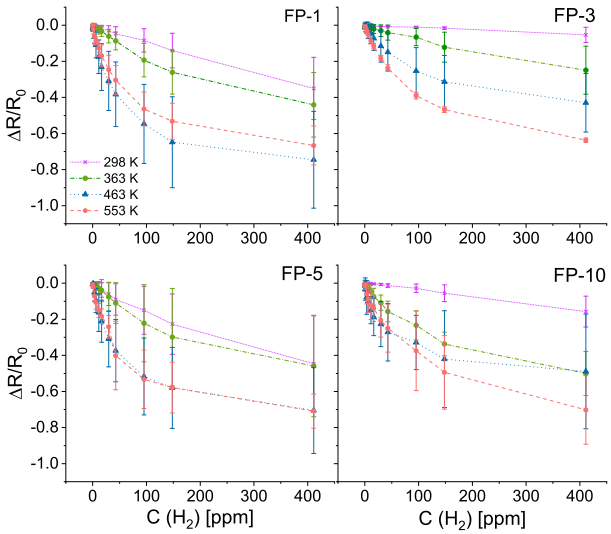

Figure 9: Response as a function of H_2 concentration of FP-1, FP-3, FP-5, and FP-10 at different temperatures. The error bars represent the standard deviation of the results of three repeated measurements at the same concentrations. See Sec. 3.4 for more details.

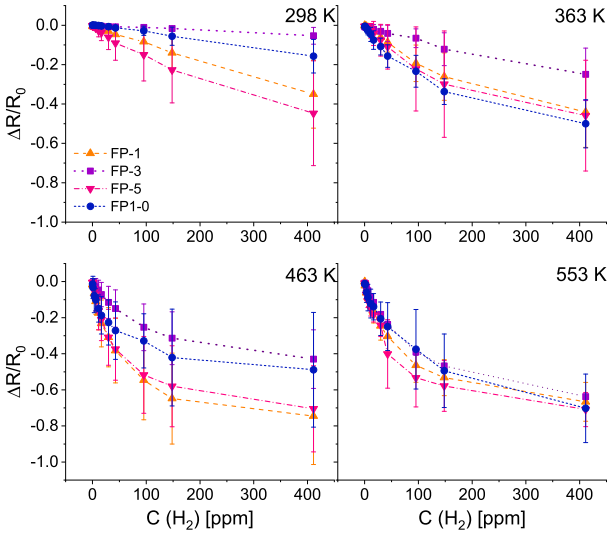

Figure 10: Response as a function of H_2 concentration for FP-1, FP-3, FP-5, and FP-10 at 298 K, 363 K, 463 K, and 553 K. The error bars represent the standard deviation of the results of three repeated measurements at the same concentrations. See Sec. 3.4 for more details.

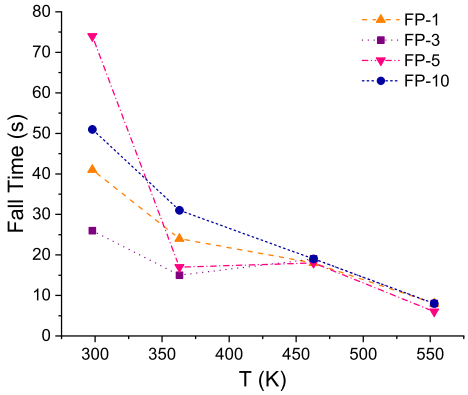

Figure 11: Average fall times of electrical resistance for samples FP-1, FP-3, FP-5, and FP-10 at different temperatures. See Sec. 3.4 for more details.

For clarification, Fig. 9 shows the comparison between the responses of a particular series of samples (FP-1, FP-3, FP-5, and FP-10) at 298 K, 363 K, 463 K, and 553 K, while Fig. 10 shows the comparison between the sample series at a specific temperature. The error bars represent the standard deviation of results obtained from repeated measurements performed at the same concentrations.

To determine the limit of detection (LOD), we take into account the noise of the measured resistance and find the lowest H_2 concentration at which the drop in

electrical resistance is at least three times as large as the noise. In this way, we estimated the LOD and to be ~8 ppm.

As mentioned in Sec. 2.5, the H_2 concentration was successively increased in steps. A step between 30 ppm and 43 ppm was chosen as a reference for the calculation and comparison of the fall times of the electrical resistance between the sample series. The comparison of the average fall times for different sample series and at different temperatures is shown in Fig. 11. It can be seen from the graph that all the sensors investigated work faster at higher temperatures. However, the plateaus at 298 K could not be reached as the sensors responded extremely slowly. Therefore, the values for the fall time at 298 K should be considered as lower limits.

4. Discussion

α-Fe_2O_3 is a surface-controlled sensor and works at low to medium temperatures (<600°C). MOS-based gas sensors primarily detect the presence of gases by monitoring the change in their electrical properties upon contact with the target gas. As described in Goel et al. (2022), the mechanisms of gas sensing can be divided into a microscopic and a macroscopic level. At the microscopic level, mechanisms such as Fermi-level control theory and charge carrier depletion layer theory are explored, but macroscopic mechanisms are usually favoured to explain gas sensing in MOS-based sensors, including adsorption/desorption processes.

Figures 9 and 10 show that the electrical resistance of the sensors decreases with increasing H_2 concentration in all cases, indicating that the interaction of H_2 gas with the sensor material (Pt/α-Fe_2O_3) increases its conductivity. This behavior is characteristic of n-type semiconductor materials, as reported by Moseley (1992); Barsan and Weimar (2003). Direct contact between the gas and the sensor triggers a chemical reaction that leads to a change in the electrical signal. This change can be attributed to the presence of the target gas or oxygen molecules in the environment (air). In general, adsorption and desorption processes describe how the behavior of the sensor changes physically or chemically when it comes into contact with the gas on its surface. When target gas molecules are present, the resistance of the material changes due to significant changes in charge carrier concentration. These concentration shifts result from the chemisorption and physisorption of target gas molecules and oxygen molecules from the air.

Oxygen adsorption is a widely used mechanism in gas sensing. which has a significant impact on most MOS-based gas sensors Liu et al. (2017b); Goel et al. (2022). When a MOS-based sensor such as α-Fe_2O_3 is exposed to air at operating temperature, oxygen molecules can be adsorbed on the surface of α-Fe_2O_3. Due to their stronger electron affinity, adsorbed oxygen molecules can be ionized into adsorbed oxygen ions by capturing free electrons from α-Fe_2O_3. The process can be described by the following reactions:

$$O_2(\text{gas}) \longrightarrow O_2(\text{ads}) \quad (1)$$
$$O_2(\text{ads}) + e^- \longrightarrow {O_2}^-(\text{ads}) \quad (2)$$
$${O_2}^-(\text{ads}) + e^- \longrightarrow 2\,O^-(\text{ads}) \quad (3)$$
$$O^-(\text{ads}) + e^- \longrightarrow O^{2-}(\text{ads}) \quad (4)$$

This process leads to a depletion of electrons, which increases the resistance of the sensor. If, on the other hand, the sensor is exposed to a reducing atmosphere, such as hydrogen gas, the previously adsorbed oxygen ions react with hydrogen gas molecules. In this reaction, the electrons are injected into the conduction band, reducing the potential barrier, which leads to a decrease in the resistance of the n-type semiconductor sensor (Moseley, 1992; Dey, 2018). The same mechanism is described in Wang et al. (2007) and also in Guo et al. (2018). Therefore, chemical adsorption is recognised as the primary gas sensing mechanism in most MOS-based gas sensors.

Our sample of pure hematite (FP-0) showed no response to hydrogen, but there are many methods to improve the sensitivity of the sensor. Apart from the fact that the sample needs to be heated, one of the methods is decoration with noble metals such as Pt, Pd, Au, Ag and others. In a recent review, Goel et al. (2022) gave an overview of the methods to improve gas sensing. They described how decoration with noble metal leads to an increase in the adsorption capacity of gases. Improving the adsorption of target gas molecules on the sensor surface can significantly increase the performance of the sensor by increasing the availability of adsorption sites. An effective and widely used method is the incorporation of noble metals into MOS sensor materials. The addition of noble metals reduces the activation energy required for adsorption and facilitates the binding of additional oxygen anions and target gas molecules (Zhou et al., 2018; Goel et al., 2022). In addition, the formation of a Schottky barrier at the interface changes the movement of the charge carriers. The so-called spillover effect, which is also described by Maosong et al. (2001) and Xue et al. (2021), reduces the activation energy of the process.

Wang et al. (2007), Liu et al. (2017a) and Guo et al. (2018) investigated the influence of platinum decoration on gas sensor performances. The Fig. 9 shows

that there is no clear dependence of the sensitivity of the sensors on the Pt concentration. However, since no response to H_2 was observed in the FP-0 sample series (samples without Pt), in our study the presence of dispersed Pt is the key component that makes α-Fe_2O_3 an H_2 sensor. Platinum can provide new sites for oxygen adsorption and can also target gas molecules. Due to the spillover effect, adsorbed oxygen species and target gas molecules can spill over onto the surface of the α-Fe_2O_3 support. Pt is therefore not involved in the electron exchange between the sensor and the target gas, but accelerates it (Wang et al., 2007). Moreover, since Pt has a higher work function (5.65 eV) than α-Fe_2O_3 (4.39 eV) (Liu et al., 2017a), electrons are transferred from α-Fe_2O_3 to Pt, which increases the depletion layer and improves the sensor performance. Since the work function of MOS is generally lower than that of noble metals, redistribution of charge is required to achieve equilibrium. Once physical contact between MOS and noble metal is established, charge transfer at the interface results in band bending, forming a Schottky barrier at the junction between MOS and noble metal. Electrons from the conduction band of the MOS migrate into the noble metal particles and form a dipole layer at the interface. This interface layer prevents the recombination of electron-hole pairs, and thus increases the gas response of the sensors. This phenomenon is called electronic sensitization (Goel et al., 2022).

Considering that all samples with Pt show a decrease in resistance when exposed to H_2, there may be a threshold Pt concentration below 1 mol% that "turns on" the sensing mechanism; determining this threshold may be the subject of future research. This suggests that sensors based on Pt/α-Fe_2O_3 are economically feasible due to a the relatively low Pt concentration required.

As can be seen from Figs. 10 and 11, all sample series show a significantly higher sensitivity and lower response times at higher temperatures. This could indicate that the reaction of H_2 with PtNPs is more efficient at higher temperatures. The increase in sensitivity with increasing temperature is a common feature of metal oxide semiconductor sensors (e.g. Watson (1984); Barsan et al. (2007); Bochenkov and Sergeev (2010); Goel et al. (2022)). The response of the sensors decreases exponentially with H_2 concentration, indicating saturation. This is further evidence that there are a limited number of sites with which H_2 can interact (Srivastava et al., 1994).

The change in resistance of the samples studied in this work is reversible (see Fig.8), i.e. after exposure to air in the absence of H_2, their resistance returns to a value similar to that before exposure to H_2. This could indicate the occurrence of reversible chemisorption. In general, chemisorption is considered as irreversible, but it has been shown that it can also be a reversible process: as mentioned by Guerrero-Ruiz (1993), this behavior has also been observed in the chemisorption of hydrogen on different catalysts, including Ir/Al_2O_3, Pt/Al_2O_3, Pt/SiO_2 and Pt/carbon. Some authors suggest that the reversibility of hydrogen chemisorption can be influenced by the experimental conditions, such as pumping speed, temperature, active surface area, etc. (Crucq et al., 1983). In contrast to this view, some researchers suggest a relationship between reversibility and the interaction of hydrogen with the platinum surface. As discussed by Prado-Burguete et al. (1991), the adsorption of hydrogen on dispersed metals such as platinum indicates the presence of both weak and strong chemisorption. In their study, they demonstrated that chemisorbed hydrogen is desorbed at 298 K by evacuation. However, in our study, reversible chemisorption of hydrogen was observed over a temperature range from room temperature to 553 K.

In their work, Maosong et al. (2001) described the influence of phase transformations on the resistance of MOS-based gas sensors. For example, α-Fe_2O_3 and γ-Fe_2O_3 are the two different crystalline phases of Fe_2O_3 and have different gas sensor properties despite their identical morphological structures. It would be helpful to compare the gas sensor properties of hematite (α-Fe_2O_3) and magnetite (Fe_3O_4) with the same morphology. Apart from the previously described noble metal decoration applied to improve the performance of gas sensor, Xu et al. (2021) explained in their research how changing the shape of the nanostructures also affects the gas sensor properties.

In our study, we found that the Pt/α-Fe_2O_3 samples show no dependence on platinum loading, although the addition of platinum is crucial. Our results suggest that even a loading of less than 1 mol% platinum is sufficient to make the material a hydrogen sensor. On the other hand, the same Pt/α-Fe_2O_3 samples in previous studies (Marić et al., 2023) showed an increase in the rate constant for the catalytic reduction of 4-NP to 4-AP in the order 5 mol% > 3 mol% > 1 mol% added platinum, indicating that improved catalytic performance is not necessarily accompanied by a higher sensitivity for H_2 sensing.

The response and response time of the sensor at an H_2 concentrations of 100 ppm ranged from ∼-10% and $\gtrapprox$75 s at 298 K to ∼-50% and ∼5 s at 553 K. This result is comparable to the response reported by Umar et al. (2021) (71%). However, they heated their sensors to a much higher temperature of 673 K. The behavior of

our sensors suggests a reversible sensing mechanism based on the Pt-mediated interaction of H_2 with adsorbed oxygen. With the low detection limit of ~8 ppm, our results are comparable to CoO_4/SnO_2-based sensors from Huo et al. (2017) (6.8 ppm), NiO nanosheets from Nakate et al. (2020) and Pd decorated MnO_2 nanowalls from Sanger et al. (2016). All these sensors are based on MOS materials and have a similar detection range as ours. Our results indicate a possible use of Pt/α-Fe_2O_3 as a sensor for H_2 with a linear response at concentrations of 0-100 ppm and encourage further research.

5. Conclusion

We have shown that the mechanochemical dispersion of 1-10 mol% Pt nanoparticles on a α-Fe_2O_3 support results in a material with chemiresistive properties that can be used to detect H_2 in ambient air. Since pure α-Fe_2O_3 does not exhibit similar sensitivity to H_2, platinum was found to be a key component for the development of H_2 sensing properties in this system. Remarkably, increasing the Pt concentration in the applied range of 1-10 mol% had no clearly discernible effect on the sensitivity of the samples for the detection of H_2, suggesting that further reduction of the Pt concentration is possible without compromising sensor performance.

Increasing the temperature significantly improves the sensitivity of all Pt-containing samples: at a H_2 concentration of 100 ppm, the sensor response and response time ranged from approximately ~-10% and $\gtrsim$75 s at 298 K to approximately ~-50% and ~5 s at 553 K, respectively. As a function of the H_2 concentration, the response of the sensors showed saturation at 400 ppm H_2.

After exposure to air in the absence of H_2, the resistance of the samples returned to a value similar to that measured before exposure to H_2. This indicates a reversible sensing mechanism that appears to be based on the Pt-mediated interaction of H_2 with oxygen adsorbed on α-Fe_2O_3.

Overall, the investigated system shows promising properties that can be further optimized for potential applications in the field of chemiresistive H_2 sensors.

6. Acknowledgements

This work was financially supported by Croatian Science Foundation under the project IP-2019-04-1195 “Platinum decorated iron tin oxide solid solutions for hydrogen gas sensing“ (HydGasSens) and by Croatian Government and the European Union through the European Regional Development Fund - the Competitiveness and Cohesion Operational Programme (KK.01.1.1.01.0001). Financial support provided by the Hungarian National Research, Development, and Innovation Office (NKFIH), grant number 2019-2.1.11-TÉT-2020-00221 is furthermore acknowledged.

References

An, N., Yu, Q., Liu, G., Li, S., Jia, M., Zhang, W., 2011. Complete oxidation of formaldehyde at ambient temperature over supported Pt/Fe_2O_3 catalysts prepared by colloid-deposition method. Journal of Hazardous Materials 186, 1392–1397. URL: https://www.sciencedirect.com/science/article/pii/S0304389410015980, doi:10.1016/j.jhazmat.2010.12.018.

Archer, D., 2008. Checking the thermostat. Nature Geoscience 1, 289–290. URL: https://www.nature.com/articles/ngeo194, doi:10.1038/ngeo194.

Aroutiounian, V., 2007. Metal oxide hydrogen, oxygen, and carbon monoxide sensors for hydrogen setups and cells. International Journal of Hydrogen Energy 32, 1145 – 1158. doi:https://doi.org/10.1016/j.ijhydene.2007.01.004.

Baran, N., Renka, S., Raić, M., Ristić, D., Ivanda, M., 2022. Effects of Thermal Oxidation on Sensing Properties of Porous Silicon. Chemosensors 10, 349. URL: https://www.mdpi.com/2227-9040/10/9/349, doi:10.3390/chemosensors10090349.

Barsan, N., Koziej, D., Weimar, U., 2007. Metal oxide-based gas sensor research: How to? Sensors and Actuators B: Chemical 121, 18–35. URL: https://www.sciencedirect.com/science/article/pii/S0925400506006204, doi:10.1016/j.snb.2006.09.047.

Barsan, N., Weimar, U., 2003. Understanding the fundamental principles of metal oxide based gas sensors; the example of CO sensing with SnO_2 sensors in the presence of humidity. Journal of Physics: Condensed Matter 15, R813–R839. URL: https://doi.org/10.1088/0953-8984/15/20/201, doi:10.1088/0953-8984/15/20/201.

Berner, R.A., 2003. The long-term carbon cycle, fossil fuels and atmospheric composition. Nature 426, 323–326. URL: https://www.nature.com/articles/nature02131, doi:10.1038/nature02131.

Bersani, D., Lottici, P.P., Montenero, A., 1999. Micro-Raman investigation of iron oxide films and powders produced by sol–gel syntheses. Journal of Raman Spectroscopy 30, 355–360. URL: https://onlinelibrary.wiley.com/doi/abs/10.1002/%28SICI%291097-4555%28199905%2930%3A5%3C355%3A%3AAID-JRS398%3E3.0.CO%3B2-C, doi:10.1002/(SICI)1097-4555(199905)30:5<355::AID-JRS398>3.0.CO;2-C.

Bochenkov, V., Sergeev, G., 2010. Sensitivity, selectivity, and stability of gas-sensitive metal-oxide nanostructures. Metal Oxide Nanostructures and Their Applications 3, 31–52.

Chamritski, I., Burns, G., 2005. Infrared- and Raman-Active Phonons of Magnetite, Maghemite, and Hematite: A Computer Simulation and Spectroscopic Study. The Journal of Physical Chemistry B 109, 4965–4968. URL: https://doi.org/10.1021/jp048748h, doi:10.1021/jp048748h.

Crucq, A., Lienard, G., Degols, L., Frennet, A., 1983. Hydrogen adsorption on Rh. Applications of Surface Science 17, 79–96. URL: https://www.sciencedirect.

com/science/article/pii/0378596383901137, doi:10.1016/0378-5963(83)90113-7.

Dey, A., 2018. Semiconductor metal oxide gas sensors: A review. Materials Science and Engineering: B 229, 206–217. doi:https://doi.org/10.1016/j.mseb.2017.12.036.

Doney, S.C., Fabry, V.J., Feely, R.A., Kleypas, J.A., 2009. Ocean Acidification: The Other CO2 Problem. Annual Review of Marine Science 1, 169–192. URL: https://www.annualreviews.org/content/journals/10.1146/annurev.marine.010908.163834, doi:10.1146/annurev.marine.010908.163834.

Duoc, V.T., Nguyen, H., Ngoc, T.M., Xuan, C.T., Hung, C.M., Duy, N.V., Hoa, N.D., 2024. Hydrogen gas sensor based on self-heating effect of SnO2/Pt thin film with ultralow power consumption. International Journal of Hydrogen Energy 61, 774–782. URL: https://www.sciencedirect.com/science/article/pii/S0360319924006025, doi:10.1016/j.ijhydene.2024.02.180.

Falkowski, P., Scholes, R.J., Boyle, E., Canadell, J., Canfield, D., Elser, J., Gruber, N., Hibbard, K., Högberg, P., Linder, S., Mackenzie, F.T., Moore III, B., Pedersen, T., Rosenthal, Y., Seitzinger, S., Smetacek, V., Steffen, W., 2000. The Global Carbon Cycle: A Test of Our Knowledge of Earth as a System. Science 290, 291–296. URL: https://www.science.org/doi/10.1126/science.290.5490.291, doi:10.1126/science.290.5490.291.

de Faria, D.L.A., Venâncio Silva, S., de Oliveira, M.T., 1997. Raman microspectroscopy of some iron oxides and oxyhydroxides. Journal of Raman Spectroscopy 28, 873–878. URL: https://onlinelibrary.wiley.com/doi/abs/10.1002/%28SICI%291097-4555%28199711%2928%3A11%3C873%3A%3AAID-JRS177%3E3.0.CO%3B2-B, doi:10.1002/(SICI)1097-4555(199711)28:11<873::AID-JRS177>3.0.CO;2-B.

Ghule, B.G., Shinde, N.M., Raut, S.D., Gore, S.K., Shaikh, S.F., Ekar, S.U., Ubaidullah, M., Pak, J.J., Mane, R.S., 2022. Self-assembled α-fe$_2$o$_3$-GO nanocomposites: Studies on physical, magnetic and ammonia sensing properties. Materials Chemistry and Physics 278, 125617. URL: https://www.sciencedirect.com/science/article/pii/S0254058421014000, doi:10.1016/j.matchemphys.2021.125617.

Goel, N., Kunal, K., Kushwaha, A., Kumar, M., 2022. Metal oxide semiconductors for gas sensing. Engineering Reports 5, e12604. URL: https://onlinelibrary.wiley.com/doi/abs/10.1002/eng2.12604, doi:10.1002/eng2.12604.

Gu, H., Wang, Z., Hu, Y., 2012. Hydrogen Gas Sensors Based on Semiconductor Oxide Nanostructures. Sensors 12, 5517–5550. URL: https://www.mdpi.com/1424-8220/12/5/5517, doi:10.3390/s120505517.

Guerrero-Ruiz, A., 1993. Some aspects of reversible chemisorption on supported platinum catalysts. Reaction Kinetics and Catalysis Letters 49, 53–60. URL: https://doi.org/10.1007/BF02084028, doi:10.1007/BF02084028.

Guinotte, J.M., Fabry, V.J., 2008. Ocean Acidification and Its Potential Effects on Marine Ecosystems. Annals of the New York Academy of Sciences 1134, 320–342. URL: https://onlinelibrary.wiley.com/doi/abs/10.1196/annals.1439.013, doi:10.1196/annals.1439.013.

Guo, L., Xie, N., Wang, C., Kou, X., Ding, M., Zhang, H., Sun, Y., Song, H., Wang, Y., Lu, G., 2018. Enhanced hydrogen sulfide sensing properties of Pt-functionalized α-Fe_2O_3 nanowires prepared by one-step electrospinning. Sensors and Actuators B: Chemical 255, 1015–1023. URL: https://www.sciencedirect.com/science/article/pii/S0925400517312637, doi:10.1016/j.snb.2017.07.055.

Hara, K., Nishida, N., 1994. H2 sensors using Fe_2O_3-based thin film. Sensors and Actuators B: Chemical 20, 181–186. URL: https://www.sciencedirect.com/science/article/pii/0925400594011818, doi:10.1016/0925-4005(94)01181-8.

Huo, L., Yang, X., Liu, Z., Tian, X., Qi, T., Wang, X., Yu, K., Sun, J., Fan, M., 2017. Modulation of potential barrier heights in Co3O4/SnO2 heterojunctions for highly H2-selective sensors. Sensors and Actuators B: Chemical 244, 694–700. URL: https://www.sciencedirect.com/science/article/pii/S0925400517300709, doi:10.1016/j.snb.2017.01.061.

Hübert, T., Boon-Brett, L., Black, G., Banach, U., 2011. Hydrogen sensors – A review. Sensors and Actuators B: Chemical 157, 329–352. URL: https://www.sciencedirect.com/science/article/pii/S0925400511003674, doi:10.1016/j.snb.2011.04.070.

Jubb, A.M., Allen, H.C., 2010. Vibrational Spectroscopic Characterization of Hematite, Maghemite, and Magnetite Thin Films Produced by Vapor Deposition. ACS Applied Materials & Interfaces 2, 2804–2812. URL: https://doi.org/10.1021/am1004943, doi:10.1021/am1004943.

Kaliyaraj Selva Kumar, A., Zhang, Y., Li, D., Compton, R.G., 2020. A mini-review: How reliable is the drop casting technique? Electrochemistry Communications 121, 106867. URL: https://www.sciencedirect.com/science/article/pii/S1388248120302186, doi:10.1016/j.elecom.2020.106867.

Klencsár, Z., Kuzmann, E., Vértes, A., 1996. User-friendly software for mössbauer spectrum analysis. Journal of Radioanalytical and Nuclear Chemistry Articles 210, 105–118. doi:10.1007/bf02055410.

Koo, W.T., Cho, H.J., Kim, D.H., Kim, Y.H., Shin, H., Penner, R.M., Kim, I.D., 2020. Chemiresistive Hydrogen Sensors: Fundamentals, Recent Advances, and Challenges. ACS Nano 14, 14284–14322. URL: https://doi.org/10.1021/acsnano.0c05307, doi:10.1021/acsnano.0c05307.

Korotcenkov, G., Han, S.D., Stetter, J.R., 2009. Review of Electrochemical Hydrogen Sensors. Chemical Reviews 109, 1402–1433. URL: https://doi.org/10.1021/cr800339k, doi:10.1021/cr800339k.

Kraushofer, F., Jakub, Z., Bichler, M., Hulva, J., Drmota, P., Weinold, M., Schmid, M., Setvin, M., Diebold, U., Blaha, P., Parkinson, G.S., 2018. Atomic-Scale Structure of the Hematite α-$Fe_2O_3(1\bar{1}02)$ "R-Cut" Surface. The Journal of Physical Chemistry C 122, 1657–1669. URL: https://doi.org/10.1021/acs.jpcc.7b10515, doi:10.1021/acs.jpcc.7b10515.

Lei, Z., Cheng, P., Wang, Y., Xu, L., Lv, L., Li, X., Sun, S., Hao, X., Zhang, Y., Zhang, Y., Weng, Z., 2023. Pt-doped α-Fe_2O_3 mesoporous microspheres with low-temperature ultra-sensitive properties for gas sensors in diabetes detection. Applied Surface Science 607, 154558. URL: https://www.sciencedirect.com/science/article/pii/S0169433222020906, doi:10.1016/j.apsusc.2022.154558.

Lewis, B., von Elbe, G., 1987. Combustion, flames and explosions of gases, in: Lewis, B., von Elbe, G. (Eds.), Combustion, Flames and Explosions of Gases. Academic Press, San Diego. URL: https://www.sciencedirect.com/science/article/pii/B9780124467514500019, doi:10.1016/B978-0-12-446751-4.50001-9.

Li, Y., Dang, J., Ma, Y., Ma, H., 2023. Hematite: A Good Catalyst for the Thermal Decomposition of Energetic Materials and the Application in Nano-Thermite. Molecules 28, 2035. URL: https://www.mdpi.com/1420-3049/28/5/2035, doi:10.3390/molecules28052035.

Li, Z., Yao, Z., Haidry, A.A., Plecenik, T., Xie, L., Sun, L., Fa-

tima, Q., 2018. Resistive-type hydrogen gas sensor based on TiO2: A review. International Journal of Hydrogen Energy 43, 21114–21132. URL: https://www.sciencedirect.com/science/article/pii/S0360319918328970, doi:10.1016/j.ijhydene.2018.09.051.

Lim, I.S., Jang, G.E., Kim, C.K., Yoon, D.H., 2001. Fabrication and gas sensing characteristics of pure and Pt-doped γ-Fe_2O_3 thin film. Sensors and Actuators B: Chemical 77, 215–220. URL: https://www.sciencedirect.com/science/article/pii/S0925400501007134, doi:10.1016/S0925-4005(01)00713-4.

Liu, C., Gao, H., Wang, L., Wang, T., Yang, X., Sun, P., Gao, Y., Liang, X., Liu, F., Song, H., Lu, G., 2017a. Facile synthesis and the enhanced sensing properties of Pt-loaded α-Fe_2O_3 porous nanospheres. Sensors and Actuators B: Chemical 252, 1153–1162. URL: https://www.sciencedirect.com/science/article/pii/S0925400517310274, doi:10.1016/j.snb.2017.06.012.

Liu, H., Choe, H.S., Chen, Y., Suh, J., Ko, C., Tongay, S., Wu, J., 2017b. Variable range hopping electric and thermoelectric transport in anisotropic black phosphorus. Applied Physics Letters 111, 102101. URL: https://aip.scitation.org/doi/full/10.1063/1.4985333, doi:10.1063/1.4985333.

Luna, C., Cuan-Guerra, A.D., Barriga-Castro, E.D., Núñez, N.O., Mendoza-Reséndez, R., 2016. Confinement and surface effects on the physical properties of rhombohedral-shape hematite (α-Fe_2O_3) nanocrystals. Materials Research Bulletin 80, 44–52. URL: https://www.sciencedirect.com/science/article/pii/S0025540816301374, doi:10.1016/j.materresbull.2016.03.029.

Ma, J., Habrioux, A., Luo, Y., Ramos-Sanchez, G., Calvillo, L., Granozzi, G., B. Balbuena, P., Alonso-Vante, N., 2015. Electronic interaction between platinum nanoparticles and nitrogen-doped reduced graphene oxide: effect on the oxygen reduction reaction. Journal of Materials Chemistry A 3, 11891–11904. URL: https://pubs.rsc.org/en/content/articlelanding/2015/ta/c5ta01285f, doi:10.1039/C5TA01285F.

Ma, L., Chen, X., Li, J., Chang, H., Schwank, J.W., 2020. Electronic metal-support interactions in Pt/FeOx nanospheres for CO oxidation. Catalysis Today 355, 539–546. URL: https://www.sciencedirect.com/science/article/pii/S0920586119303311, doi:10.1016/j.cattod.2019.06.055.

Majhi, S.M., Mirzaei, A., Kim, H.W., Kim, S.S., Kim, T.W., 2021. Recent advances in energy-saving chemiresistive gas sensors: A review. Nano Energy 79, 105369. URL: https://www.sciencedirect.com/science/article/pii/S2211285520309460, doi:10.1016/j.nanoen.2020.105369.

Maksimova, N.K., Sevastyanov, E.Y., Chernikov, E.V., Korusenko, P.M., Nesov, S.N., Kim, S.V., Biryukov, A.A., Sergeychenko, N.V., Davletkildeev, N.A., Sokolov, D.V., 2021. Sensors based on tin dioxide thin films for the detection of pre-explosive hydrogen concentrations. Sensors and Actuators B: Chemical 341, 130020. URL: https://www.sciencedirect.com/science/article/pii/S092540052100589X, doi:10.1016/j.snb.2021.130020.

Maosong, T., Guorui, D., Dingsan, G., 2001. Surface modification of oxide thin film and its gas-sensing properties. Applied Surface Science 171, 226–230. URL: https://www.sciencedirect.com/science/article/pii/S016943320000708X, doi:10.1016/S0169-4332(00)00708-X.

Marić, I., Dražić, G., Radin, E., Peter, R., Škrabić, M., Jurkin, T., Pustak, A., Baran, N., Mikac, L., Ivanda, M., Petravić, M., Štefanić, G., Gotić, M., 2023. Impact of platinum loading and dispersion on the catalytic activity of Pt/SnO2 and Pt/α-Fe_2O_3. Applied Surface Science 607, 155073. URL: https://www.sciencedirect.com/science/article/pii/S0169433222026010, doi:10.1016/j.apsusc.2022.155073.

Marshall, C.P., Dufresne, W.J., Rufledt, C.J., 2020. Polarized Raman spectra of hematite and assignment of external modes. Journal of Raman Spectroscopy 51, 1522–1529. URL: https://onlinelibrary.wiley.com/doi/abs/10.1002/jrs.5824, doi:10.1002/jrs.5824.

Moseley, P.T., 1992. Materials selection for semiconductor gas sensors. Sensors and Actuators B: Chemical 6, 149–156. URL: https://www.sciencedirect.com/science/article/pii/0925400592800472, doi:10.1016/0925-4005(92)80047-2.

Muhajir, M., Puspitasari, P., Abd Razak, J., 2019. Synthesis and Applications of Hematite α-Fe_2O_3 : a Review. Journal of Mechanical Engineering Science and Technology 3, 51–58. doi:10.17977/um016v3i22019p051.

Nakatani, Y., Matsuoka, M., 1982. Effects of Sulfate Ion on Gas Sensitive Properties of α-Fe $_2$ O $_3$ Ceramics. Japanese Journal of Applied Physics 21, L758. URL: https://iopscience.iop.org/article/10.1143/JJAP.21.L758, doi:10.1143/JJAP.21.L758.

Nakate, U.T., Ahmad, R., Patil, P., Yu, Y.T., Hahn, Y.B., 2020. Ultra thin NiO nanosheets for high performance hydrogen gas sensor device. Applied Surface Science 506, 144971. URL: https://www.sciencedirect.com/science/article/pii/S0169433219337882, doi:10.1016/j.apsusc.2019.144971.

Ogden, J.M., 2002. Hydrogen: The Fuel of the Future? Physics Today 55. URL: https://www.elibrary.ru/item.asp?id=4424392.

Ozdemir, O., Dunlop, D.J., Berquó, T.S., 2008. Morin transition in hematite: Size dependence and thermal hysteresis. Geochemistry, Geophysics, Geosystems 9. URL: https://onlinelibrary.wiley.com/doi/abs/10.1029/2008GC002110, doi:10.1029/2008GC002110.

Pathak, A.K., Verma, S., Sakda, N., Viphavakit, C., Chitaree, R., Rahman, B.M.A., 2023. Recent Advances in Optical Hydrogen Sensor including Use of Metal and Metal Alloys: A Review. Photonics 10, 122. URL: https://www.mdpi.com/2304-6732/10/2/122, doi:10.3390/photonics10020122.

Penza, M., Rossi, R., Alvisi, M., Cassano, G., Signore, M.A., Serra, E., Giorgi, R., 2008. Pt- and Pd-nanoclusters functionalized carbon nanotubes networked films for sub-ppm gas sensors. Sensors and Actuators B: Chemical 135, 289–297. URL: https://www.sciencedirect.com/science/article/pii/S0925400508005820, doi:10.1016/j.snb.2008.08.024.

Picasso, G., Sun Kou, M.R., Vargasmachuca, O., Rojas, J., Zavala, C., Lopez, A., Irusta, S., 2014. Sensors based on porous Pd-doped hematite (α-Fe_2O_3) for LPG detection. Microporous and Mesoporous Materials 185, 79–85. URL: https://www.sciencedirect.com/science/article/pii/S1387181113005714, doi:10.1016/j.micromeso.2013.11.014.

Pourmadadi, M., Rahmani, E., Shamsabadipour, A., Mahtabian, S., Ahmadi, M., Rahdar, A., Díez-Pascual, A.M., 2022. Role of Iron Oxide (Fe_2O_3) Nanocomposites in Advanced Biomedical Applications: A State-of-the-Art Review. Nanomaterials 12, 3873. URL: https://www.mdpi.com/2079-4991/12/21/3873, doi:10.3390/nano12213873.

Prado-Burguete, C., Linares-Solano, A., Rodriguez-Reinoso, F., De Lecea, C.S.M., 1991. Effect of carbon support and mean Pt particle size on hydrogen chemisorption by carbon-supported Pt

ctalysts. Journal of Catalysis 128, 397–404. URL: https://www.sciencedirect.com/science/article/pii/002195179190298I, doi:10.1016/0021-9517(91)90298-I.

Radin, E., Štefanić, G., Dražić, G., Marić, I., Jurkin, T., Pustak, A., Baran, N., Raić, M., Gotić, M., 2021. Solid-State Dispersions of Platinum in the SnO2 and Fe_2O_3 Nanomaterials. Nanomaterials 11, 3349. URL: https://www.mdpi.com/2079-4991/11/12/3349, doi:10.3390/nano11123349.

Rancourt, D.G., Ping, J.Y., 1991. Voigt-based methods for arbitrary-shape static hyperfine parameter distributions in Mössbauer spectroscopy. Nuclear Instruments and Methods in Physics Research Section B: Beam Interactions with Materials and Atoms 58, 85–97. URL: https://www.sciencedirect.com/science/article/pii/0168583X91956813, doi:10.1016/0168-583X(91)95681-3.

Reddy, M.V., Yu, T., Sow, C.H., Shen, Z.X., Lim, C.T., Subba Rao, G.V., Chowdari, B.V.R., 2007. α-Fe_2O_3 Nanoflakes as an Anode Material for Li-Ion Batteries. Advanced Functional Materials 17, 2792–2799. URL: https://onlinelibrary.wiley.com/doi/abs/10.1002/adfm.200601186, doi:10.1002/adfm.200601186.

Sanger, A., Kumar, A., Kumar, A., Chandra, R., 2016. Highly sensitive and selective hydrogen gas sensor using sputtered grown Pd decorated MnO2 nanowalls. Sensors and Actuators B: Chemical 234, 8–14. URL: https://www.sciencedirect.com/science/article/pii/S0925400516306347, doi:10.1016/j.snb.2016.04.152.

Saritas, S., Kundakci, M., Coban, O., Tuzemen, S., Yildirim, M., 2018. Ni: Fe_2O_3, Mg: Fe_2O_3 and Fe_2O_3 thin films gas sensor application. Physica B: Condensed Matter 541, 14–18. URL: https://www.sciencedirect.com/science/article/pii/S0921452618302941, doi:10.1016/j.physb.2018.04.028.

Shrisha, Wu, C.M., Motora, K.G., Chen, G.Y., Kuo, D.H., Gultom, N.S., 2023. Highly efficient reduced tungsten oxide-based hydrogen gas sensor at room temperature. Materials Science and Engineering: B 289, 116285. URL: https://www.sciencedirect.com/science/article/pii/S0921510723000272, doi:10.1016/j.mseb.2023.116285.

Srivastava, R.K., Lal, P., Dwivedi, R., Srivastava, S.K., 1994. Sensing mechanism in tin oxide-based thick-film gas sensors. Sensors and Actuators B: Chemical 21, 213–218. URL: https://www.sciencedirect.com/science/article/pii/0925400594012482, doi:10.1016/0925-4005(94)01248-2. ammonia sensing mechanisma.

Sun, B., Ding, Y., Wang, Q., Song, P., 2024. Rational design of 1D/2D heterostructured ZnSnO3/ZnO/Ti3C2TX MXene nanocomposites for enhanced acetone gas sensing performance. Sensors and Actuators B: Chemical 409, 135541. URL: https://www.sciencedirect.com/science/article/pii/S0925400524002703, doi:10.1016/j.snb.2024.135541.

Sun, B., Horvat, J., Kim, H.S., Kim, W.S., Ahn, J., Wang, G., 2010. Synthesis of Mesoporous α-Fe_2O_3 Nanostructures for Highly Sensitive Gas Sensors and High Capacity Anode Materials in Lithium Ion Batteries. The Journal of Physical Chemistry C 114, 18753–18761. URL: https://doi.org/10.1021/jp102286e, doi:10.1021/jp102286e.

Sánchez, L.C., Arboleda, J.D., Saragovi, C., Zysler, R.D., Barrero, C.A., 2007. Magnetic and structural properties of pure hematite submitted to mechanical milling in air and ethanol. Physica B: Condensed Matter 389, 145–149. URL: https://www.sciencedirect.com/science/article/pii/S0921452606015717, doi:10.1016/j.physb.2006.07.042.

T, R.B., Yadav, P.V.K., Mondal, A., Ramakrishnan, K., Jarugala, J., Liu, C., Reddy, Y.A.K., 2024. Enhanced response of WO3 thin film through Ag loading towards room temperature hydrogen gas sensor. Chemosphere 353, 141545. URL: https://www.sciencedirect.com/science/article/pii/S0045653524004387, doi:10.1016/j.chemosphere.2024.141545.

Ta, V.D., Carter, R.M., Esenturk, E., Connaughton, C., Wasley, T.J., Li, J., Kay, R.W., Stringer, J., Smith, P.J., Shephard, J.D., 2016. Dynamically controlled deposition of colloidal nanoparticle suspension in evaporating drops using laser radiation. Soft Matter 12, 4530–4536. URL: https://pubs.rsc.org/en/content/articlelanding/2016/sm/c6sm00465b, doi:10.1039/C6SM00465B.

Umar, A., Ibrahim, A.A., Kumar, R., Albargi, H., Alsaiari, M.A., Ahmed, F., 2021. Cubic shaped hematite (α-Fe_2O_3) micro-structures composed of stacked nanosheets for rapid ethanol sensor application. Sensors and Actuators B: Chemical 326, 128851. URL: https://www.sciencedirect.com/science/article/pii/S0925400520311989, doi:10.1016/j.snb.2020.128851.

Wang, H., An, K., Sapi, A., Liu, F., Somorjai, G.A., 2014. Effects of Nanoparticle Size and Metal/Support Interactions in Pt-Catalyzed Methanol Oxidation Reactions in Gas and Liquid Phases. Catalysis Letters 144, 1930–1938. URL: https://doi.org/10.1007/s10562-014-1347-9, doi:10.1007/s10562-014-1347-9.

Wang, L., Xiao, Z., Yao, X., Yu, X., Tu, S.T., Chen, S., 2023. Pt=Pd separation modified Ti3C2TX MXene for hydrogen detection at room temperature. International Journal of Hydrogen Energy 48, 30205–30217. URL: https://www.sciencedirect.com/science/article/pii/S0360319923019833, doi:10.1016/j.ijhydene.2023.04.202.

Wang, Y., Wang, S., Zhao, Y., Zhu, B., Kong, F., Wang, D., Wu, S., Huang, W., Zhang, S., 2007. H2S sensing characteristics of Pt-doped α-Fe_2O_3 thick film sensors. Sensors and Actuators B: Chemical 125, 79–84. URL: https://www.sciencedirect.com/science/article/pii/S0925400507000573, doi:10.1016/j.snb.2007.01.037.

Watson, J., 1984. The tin oxide gas sensor and its applications. Sensors and Actuators 5, 29–42. URL: https://www.sciencedirect.com/science/article/pii/0250687484870043, doi:https://doi.org/10.1016/0250-6874(84)87004-3.

Wu, D., Zhou, L., Chen, C., Liang, X., 2023. Adsorption properties of pt/n-doped graphene for sf6 decomposition species. Sens. Mater , 6.

Xie, Q., Ding, Y., Wang, Q., Song, P., 2024. Fabrication of 1D/2D In2O3 nanofibers/Ti3C2TX MXene composites for high performance detection of trimethylamine at low temperature. Sensors and Actuators B: Chemical 405, 135338. URL: https://www.sciencedirect.com/science/article/pii/S0925400524000674, doi:10.1016/j.snb.2024.135338.

Xie, S., Iglesia, E., Bell, A.T., 2001. Effects of Temperature on the Raman Spectra and Dispersed Oxides. The Journal of Physical Chemistry B 105, 5144–5152. URL: https://doi.org/10.1021/jp004434s, doi:10.1021/jp004434s.

Xu, H., Tu, X., Wang, X., Liu, X., Fan, G., 2021. Theoretical study of the adsorption and sensing properties of pure and metal doped C24N24 fullerene for its potential application as high-performance gas sensor. Materials Science in Semiconductor Processing 134, 106035. URL: https://www.sciencedirect.com/science/article/pii/S1369800121003814, doi:10.1016/j.mssp.2021.106035.

Xue, S., Cao, S., Huang, Z., Yang, D., Zhang, G., 2021. Im-

proving Gas-Sensing Performance Based on MOS Nanomaterials: A Review. Materials 14, 4263. URL: https://www.ncbi.nlm.nih.gov/pmc/articles/PMC8347970/, doi:10.3390/ma14154263.

Zhang, S., Ding, Y., Wang, Q., Song, P., 2023. MOFs-derived In2O3/ZnO/Ti3C2TX MXene ternary nanocomposites for ethanol gas sensing at room temperature. Sensors and Actuators B: Chemical 393, 134122. URL: https://www.sciencedirect.com/science/article/pii/S0925400523008377, doi:10.1016/j.snb.2023.134122.

Zhou, R., Lin, X., Xue, D., Zong, F., Zhang, J., Duan, X., Li, Q., Wang, T., 2018. Enhanced H2 gas sensing properties by Pd-loaded urchin-like W18O49 hierarchical nanostructures. Sensors and Actuators B: Chemical 260, 900–907. URL: https://www.sciencedirect.com/science/article/pii/S0925400518301047, doi:10.1016/j.snb.2018.01.104.